Diagn Interv Radiol 2026; DOI: 10.4274/dir.2026.263743

ABDOMINAL RADIOLOGY

ORIGINAL ARTICLE

Intratumoral and peritumoral radiomics based on multi-parametric magnetic resonance imaging for predicting microsatellite instability in endometrial cancer

Xiaoyu He
Xi Yin

The First Affiliated Hospital, Shihezi University, Medical Imaging Center, Shihezi, China

PURPOSE

This study aimed to evaluate the utility of intratumoral and peritumoral radiomics derived from multi-parametric magnetic resonance imaging for predicting microsatellite instability (MSI) in endometrial cancer (EC).

METHODS

We retrospectively analyzed 161 patients with pathologically confirmed EC, assigning them to a training (n = 112) and a test cohort (n = 49) at a 7:3 ratio, and collected their full clinical and imaging data. We manually delineated regions of interest on axial T2-weighted imaging (T2WI), diffusion-weighted imaging (DWI), and dynamic contrast-enhanced (CE) T1-weighted imaging sequences, expanding them by 3, 5, and 7 mm to define peritumoral regions. We then extracted and selected radiomic features from both intratumoral and peritumoral areas. Using six machine learning algorithms, we developed separate radiomics models and assessed their performance via the area under the receiver operating characteristic curve (AUC). To complete the evaluation, we compared statistical differences using the DeLong test and generated calibration curves to verify predictive accuracy.

RESULTS

Clinical characteristics exhibited no significant correlation with MSI status. In single-sequence analysis, the CE model demonstrated the highest performance (training AUC: 0.912; test AUC: 0.856). The multi-parametric model (T2WI + DWI + CE) outperformed single-sequence models, achieving AUCs of 0.934 and 0.914 in the training and test cohorts, respectively. Peritumoral radiomics independently showed robust predictive value; specifically, the model derived from 3 mm peritumoral features (across DWI) yielded a training AUC of 0.898 and a test AUC of 0.790. Notably, the integration of intratumoral and peritumoral features maximized predictive accuracy. The final model, combining optimal intratumoral features (T2WI + DWI + CE) with 3 mm peritumoral DWI features, achieved the best performance with a remarkable AUC of 0.998 in the test cohort.

CONCLUSION

Peritumoral radiomics possesses strong independent predictive value and significantly enhances the performance of intratumoral models. The integration of intratumoral and peritumoral radiomics offers a precise, non-invasive method for preoperative MSI prediction, serving as a valuable tool to facilitate clinical decision-making.

CLINICAL SIGNIFICANCE

This study establishes a reliable, non-invasive radiomics approach for the preoperative assessment of MSI status.

KEYWORDS

Endometrial cancer, microsatellite instability, peritumor, radiomics, magnetic resonance imaging, diffusion-weighted imaging, predictive model

Corresponding author: Xi Yin

E-mail: 1260431436@qq.com

Received 12 December 2025; revision requested 18 January 2026; last revision requested 21 February 2026; accepted 11 March 2026.

Epub: 12.05.2026

DOI: 10.4274/dir.2026.263743

You may cite this article as: He X, Yin X. Intratumoral and peritumoral radiomics based on multi-parametric magnetic resonance imaging for predicting microsatellite instability in endometrial cancer. *Diagn Interv Radiol*. 12 May 2026 DOI: 10.4274/dir.2026.263743 [Epub Ahead of Print].

Endometrial cancer (EC) ranks as the sixth most common cancer in women globally and stands as one of the top three gynecological malignancies. Both its incidence and mortality rates have shown a steady upward trend. In 2020, China accounted for 19.6% of global new cases of uterine malignancies and 17.1% of related deaths, underscoring the substantial burden it places on women's health.[1] Microsatellite instability (MSI), a genomic hypermutable phenotype resulting from defects in the DNA mismatch repair (MMR) system, is profoundly implicated in the progression, prognosis, and therapeutic response to anti-programmed cell death protein 1/programmed death-ligand 1 immunotherapy in EC.[2] Notably, patients with MSI-high (MSI-H) EC exhibit significantly superior responses to immunotherapy and improved prognoses compared with those with microsatellite stable (MSS) tumors.[3,4] Consequently, accurate preoperative assessment of MSI status is pivotal for tailoring individualized treatment strategies and optimizing clinical outcomes.

Currently, the gold standard for MSI detection relies on postoperative immunohistochemistry (IHC). However, this method is limited by its invasive nature, potential sampling bias, and inability to provide real-time guidance for preoperative planning.[5] As a promising non-invasive modality, magnetic resonance imaging (MRI) is widely utilized for tumor assessment due to its superior visualization of anatomical structures and tissue characteristics.[6-9] Radiomics leverages machine learning algorithms to extract high-throughput quantitative features from medical images, decoding tumor heterogeneity that is often imperceptible to visual inspection;[10] this approach has demonstrated significant value in tumor staging and therapeutic efficacy prediction.[11] Nevertheless, current radiomics investigations into EC-MSI[12-14] have predominantly focused on intratumoral features, largely overlooking the peritumoral region. The peritumoral microenvironment—characterized by inflammation, angiogenesis, and microscopic infiltration—is biologically relevant and may harbor complementary information regarding MSI status. To bridge this gap, we innovatively integrated multi-sequence MRI-based radiomic features from both intratumoral and peritumoral regions to construct a robust prediction model for MSI in EC. This study aims to establish a non-invasive, efficient method for preoperative MSI assessment, thereby providing a novel diagnostic tool to facilitate precision medicine in EC.

Main points

- Microsatellite instability (MSI) is not only significantly associated with the progression and prognosis of endometrial cancer (EC), but it also serves as a critical predictive biomarker for the efficacy of anti-programmed cell death protein 1 and anti-programmed death-ligand 1 immunotherapy.
- Accurate assessment of MSI status is a fundamental prerequisite for tailoring personalized treatment strategies and optimizing clinical outcomes in patients with EC.
- The integration of intratumoral and peritumoral imaging features offers a promising, non-invasive modality for the accurate preoperative prediction of MSI status.

Methods

Research participants

This retrospective study was approved by the Ethics Review Committee of The First Affiliated Hospital, Shihezi University (approval number: KJ2022-11-01, date: 2022.11.01), and the requirement for informed consent was waived due to the retrospective nature of the analysis. Data were collected from 161 patients with EC admitted to the study institution between January 2018 and May 2025. The cohort was randomly divided into a training set (n = 112) and a test set (n = 49) at a ratio of 7:3 using a computer-generated random number sequence. The inclusion criteria were as follows: (1) histopathologically confirmed diagnosis of EC with complete assessment of MSI status and (2) availability of standard preoperative pelvic MRI scans. Patients were excluded if they met any of the following criteria: (1) receipt of preoperative antitumor therapies, such as chemotherapy or radiotherapy, or (2) presence of significant motion artifacts or metal artifacts on MRI images that interfered with image analysis and feature extraction.

Data collection and microsatellite instability determination

Based on prior literature, the following clinical characteristics were retrieved from electronic medical records: age, body mass index (BMI), menopausal status, history of hypertension and diabetes mellitus, International Federation of Gynecology and Obstetrics stage, histological grade, deep myometrial invasion (DMI), lymphovascular space invasion (LVSI), and lymph node metastasis (LNM). MSI status was determined via IHC in strict adherence to the expert consensus guidelines on MSI detection techniques.[15] IHC staining was performed to evaluate the expression of four MMR proteins: MLH1, MSH2, MSH6, and PMS2. Tumors exhibiting loss of nuclear expression in one or more (≥ 1) of these proteins were classified as MSI-H. Conversely, tumors demonstrating intact expression of all four proteins were classified as MSS or MSI-low.

Magnetic resonance imaging acquisition protocols

Before the examination, all patients were screened for and instructed to remove metallic objects to ensure safety. To minimize intestinal motion and susceptibility artifacts, a bowel preparation protocol was implemented: Patients ingested two sachets of polyethylene glycol electrolyte powder (137.15 g per sachet dissolved in 2,000 mL of warm water) 4 hours before the scan, consuming the entire volume within 1 hour to achieve complete colonic cleansing. Following bowel preparation, patients were instructed to drink 500–800 mL of water 1 hour before imaging to maintain moderate bladder distension. An intravenous catheter was inserted into the antecubital vein for contrast administration. Patients were positioned supine, head-first, with arms raised above the head, and were trained in breath-holding techniques or instructed to breathe naturally to minimize respiratory motion artifacts.

Images were acquired using a Siemens 3.0 T magnetic resonance scanner (Siemens Healthineers, Erlangen, Germany) equipped with an 8-channel phased-array body coil. The protocol included conventional pelvic MRI sequences and dynamic contrast-enhanced (CE) MRI. Detailed scanning parameters are summarized in Table 1.

Regions of interest segmentation and feature extraction

MRI scans in Digital Imaging and Communications in Medicine format were retrieved from the Picture Archiving and Communication System and imported into the uAI research platform (Version 20250130, Shanghai United Imaging Intelligence Co., Ltd.) for analysis. Regions of interest (ROIs) were manually delineated layer-by-layer on the axial T2-weighted imaging (T2WI), diffusion-weighted imaging (DWI), and the third or fourth phase of DCE T1-weighted imaging sequences. The segmentation was performed by a radiologist with 10 years of experience in gynecological MRI, who was blinded to the patients' clinical and pathological information. The detailed workflow of this study is illustrated in Figure 1.

To evaluate inter-observer reproducibility, two radiologists with 10 and 15 years of experience in gynecologic imaging, who were blinded to clinical information, independently performed tumor ROI segmentation on 50 randomly selected cases from the training cohort. To assess intra-observer reproducibility, one of the radiologists repeated the segmentation on the same images after a washout period of 4 weeks. The intraclass correlation coefficient (ICC) was calculated for all extracted features. Only features demonstrating high stability (ICC > 0.80) were considered robust and retained for subsequent analysis.

Peritumoral ROIs were generated by dilating the manual tumor ROI boundaries by 3, 5, and 7 mm and subsequently subtracting the original intratumoral volume. Before feature extraction, images underwent standardization, resampling, and N4 bias field correction to ensure data consistency. Radiomic features were extracted from three distinct regions: the intratumoral ROI, the peritumoral ROI, and the combined (tumor + peritumoral) ROI. The extracted feature set included morphological features, first-order statistics, and texture features derived from the Gray Level Co-occurrence Matrix, Gray Level Run Length Matrix, Gray Level Size Zone Matrix, Gray Level Dependence Matrix, and Neighboring Gray Tone Difference Matrix. Data were normalized using Z-score standardization. To address overfitting, dimensionality reduction was performed using Pearson correlation analysis followed by the least absolute shrinkage and selection operator regression model with 10-fold cross-validation (Figure 2).

Model construction and nomogram evaluation

This study evaluated three MRI sequences and four distinct ROIs, comprising the intratumoral region and three peritumoral volumes defined by margins of 3, 5, and 7 mm. Following feature extraction and selection, six machine learning algorithms were employed: logistic regression, support vector machine, random forest, decision tree (DT), bagging DT (BDT), and Gaussian process. Initially, independent radiomics models were constructed for the intratumoral and peritumoral regions. The top-performing peritumoral model for each sequence was identified, and its selected features were integrated with those from the intratumoral region. These composite feature sets were then input into the optimal classifier to establish the final combined (Intratumoral + Peritumoral) model. Predictive performance was assessed via receiver operating characteristic (ROC) analysis, with the area under the curve (AUC) serving as the primary metric. Furthermore, calibration curves were plotted to assess the agreement between predicted and observed outcomes, and decision curve analysis was performed to determine the model's clinical utility.

Statistical analysis

Statistical analyses were performed using IBM SPSS Statistics for Windows, version 22.0 (IBM Corp., Armonk, NY, USA), and the United Imaging Research Platform. Continuous variables with a normal distribution were expressed as mean ± standard deviation and compared using the independent samples *t*-test. Non-normally distributed variables were reported as the median with interquartile range and analyzed using the Mann–Whitney U test. Categorical variables were presented as frequencies and percentages [n (%)] and compared using the chi-square test or Fisher's exact test, as appropriate. The DeLong test was employed to compare differences in the AUCs between models. A P value < 0.05 was considered statistically significant.

Results

Demographic and clinical characteristics

A total of 161 patients with EC were enrolled in this study, comprising 33 in the MSI group and 128 in the MSS group. Patients were assigned to a training cohort (n = 112) and a test cohort (n = 49) at a ratio of 7:3. As shown in Table 2, there were no statistically significant differences between the training and test cohorts regarding baseline clinical characteristics, including age, BMI, menopausal status, comorbidities (hypertension or diabetes), or tumor pathological features

Table 1. Magnetic resonance imaging scanning parameters

Parameters	TR/TE (ms)	Slice thickness (mm)	Interlayer spacing (mm)	Matrix
T2WI-FRFSE	6,377/92	5	1	352 × 320
DWI	4,700/65	5	1	256 × 192
DCE	4.6/MinFull	3	1	320 × 200

T2WI-FRFSE, T2-weighted imaging-fast recovery fast spin echo; TR, repetition time; TE, echo time; DWI, diffusion-weighted imaging; DCE, dynamic contrast-enhanced magnetic resonance imaging; MinFull, minimum full.

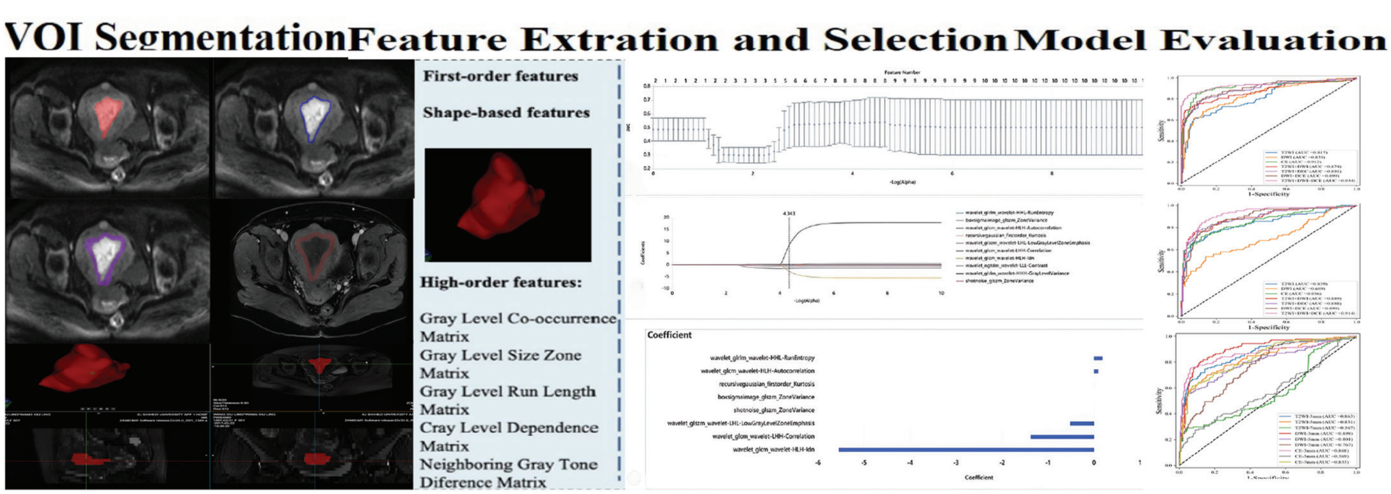

Figure 1. Overview of the study. VOI, volume of interest.

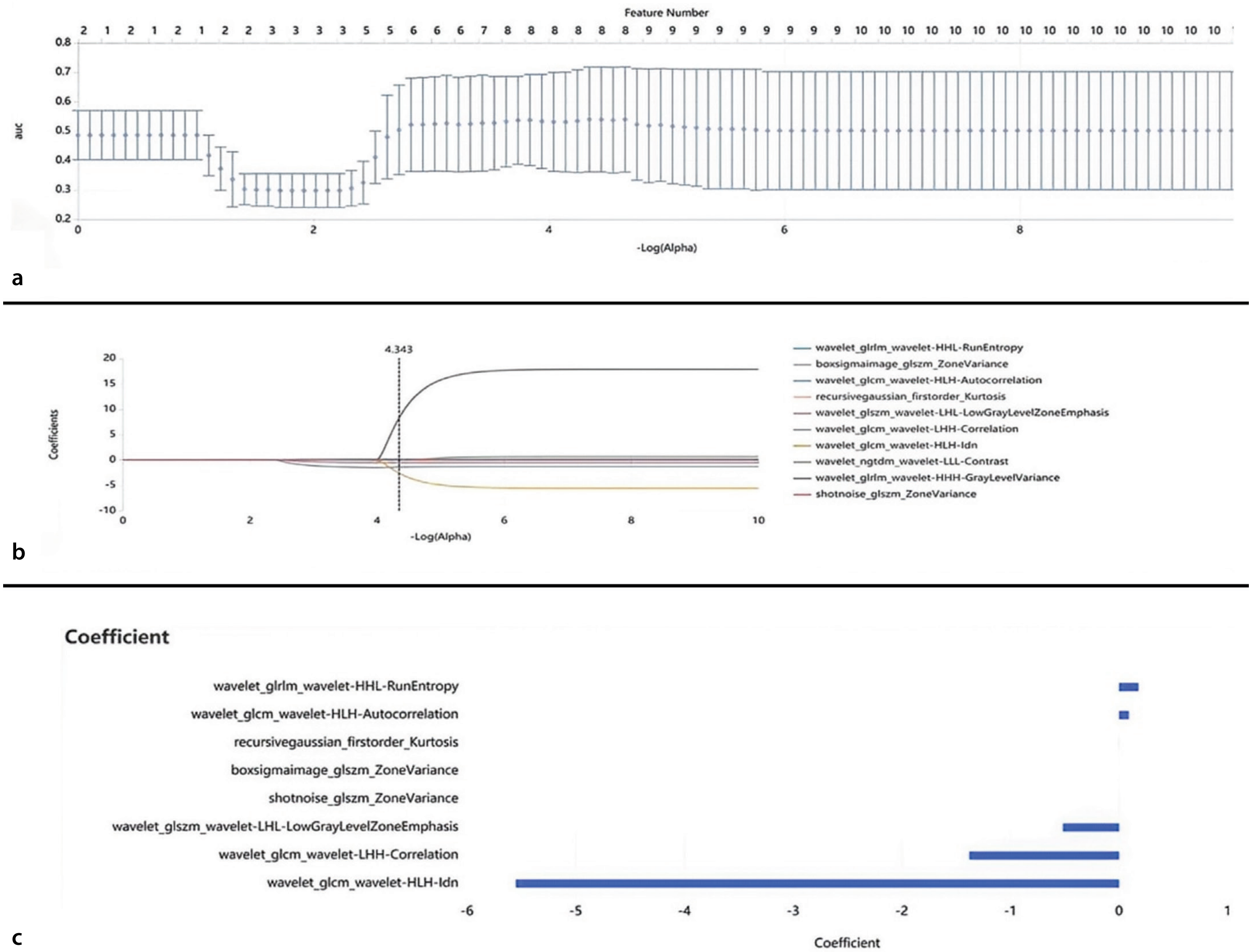

Figure 2. (a–c): LASSO screening of radiomic features related to MSI. **(a)** Optimal hyperparameter values were found through 10-fold cross-validation; **(b)** Relationship diagram of different texture feature coefficients with changes; **(c)** LASSO coefficient values of the selected features. LASSO, Least Absolute Shrinkage and Selection Operator; MSI, microsatellite instability.

Table 2. Comparison of clinical information between the training group and the test group of patients

Parameters	Training group (n = 112)	Test group (n = 49)	t/x^2	*P*
Age (years)	49.57 ± 7.28	48.53 ± 8.05	0.821[1]	0.307
BMI (kg/m²)	24.16 ± 2.31	23.32 ± 2.01	0.211[1]	0.402
Hypertension			3.001	0.487
With/without	60/52	25/24		
Diabetes			0.201	0.538
With/without	27/85	12/37		
Tumor stage			0.231	0.135
I+II/III+IV	97/15	43/6		
Tumor grade			1.423	0.332
G1 + G2/G3	82/30	37/12		
DMI			1.673	0.278
(−)/(+)	90/22	45/4		

The values marked with superscript (1) represent statistical results analyzed by the independent sample t-test. BMI, body mass index; DMI, deep myometrial infiltration; G1/G2/G3, tumor differentiation grade.

(stage, grade, DMI, LVSI, and LNM) ($P > 0.05$). This indicates a balanced distribution of data between the two sets. Furthermore, univariate and multivariate analyses of clinical variables in the training cohort revealed no independent predictors significantly associated with MSI status (Table 3).

Establishment of radiomics models

A total of 1,904 radiomic features were extracted from the intratumoral region, the peritumoral regions (defined by 3, 5, and 7 mm margins), and the combined intratumoral–peritumoral regions. Comparative analysis using ROC curves across six classifiers demonstrated that the BDT achieved the highest AUC and exhibited superior stability.

Table 3. Univariate and multivariate logistic regression analysis of the training group

Parameters	MSI	MSS	Univariate analysis		Multivariable analysis	
	n = 33	n = 128	OR (95% CI)	*P*	OR (95% CI)	*P*
Age (years)	50.31 ± 1.04	52.07 ± 1.01	0.947 (0.821–1.082)	< 0.05	0.743 (0.617–1.013)	0.512
BMI (kg/m^2)	24.18 ± 0.11	23.41 ± 1.34	1.563 (1.340–2.041)	0.301		
Hypertension			1.784 (1.224–2.101)	0.813		
With/without	17/16	65/63				
Diabetes			12.300 (12.120–15.102)	0.013		
With/without	8/25	33/95				
Tumor stage				0.110		
I+II/III+IV	28/5	113/15	4.005 (3.783–4.111)			
Tumor grade				0.223		
G1 + G2/G3	24/9	98/30	4.115 (4.114–6.234)			
DMI				0.112		
(−)/(+)	26/7	118/10	9.894 (8.110–11.211)			

MSI, microsatellite instability; MSS, microsatellite stability; OR, odds ratio; CI, confidence interval; BMI, body mass index; DMI, deep myometrial infiltration; G1/G2/G3, tumor differentiation grade.

Table 4. Area under the receiver operating characteristic curve of 42 intra-tumoral radiomic features in the training group and the test group

	T2WI	DWI	DCE	T2WI +DWI	T2WI +DCE	DWI +DCE	T2WI+DWI +DCE
LR	0.977 (0.909–1)	1 (1–1)	0.646 (0.593–0.876)	1 (1–1)	1 (1–1)	1 (1–1)	1 (1–1)
	0.354 (0.726–0.782)	0.5556 (0.037–1)	0.719 (0.214–0.745)	0.645 (0.426–1)	0.499 (0.037–1)	0.501 (0.040–1)	0.787 (0.073–1)
BDT	0.817 (0.801–0.954)	0.835 (0.794–0.997)	0.912 (0.756–0.967)	0.874 (0.799–1)	0.891 (0.776–1)	0.899 (0.997–1)	0.934 (0.814–0.957)
	0.839 (0.686–0.902)	0.6889 (0.795–1)	0.856 (0.721–1)	0.889 (0.545–1)	0.888 (0.845–1)	0.889 (0.864–1)	0.914 (0.789–0.954)
DT	0.754 (0.632–0.875)	0.804 (0.685–0.923)	0.754 (0.617–0.836)	0.804 (0.598–0.932)	0.804 (0.701-0.903)	0.804 (0.770–0.912)	0.960 (0.685–0.973)
	0.4194 (0.307–0.531)	0.688 (0.140–1)	0.950 (0.435–1)	0.690 (0.351–1)	0.701 (0.298–1)	0.693 (0.303–1)	0.6760 (0.013–1)
GP	0.654 (0.489–0.81)	0.728 (0.580–0.875)	0.654 (0.566–0.831)	0.728 (0.580–0.875)	0.728 (0.580–0.875)	0.728 (0.580–0.875)	0.772 (0.050–0.784)
	0.6774 (0.219–1)	0.777 (0.475–1)	0.702 (0.419–0.721)	0.603 (0.085–1)	0.806 (0.564–1)	0.572 (0.483–1)	0.709 (0.364–1)
RF	0.999 (0.999–1)	1 (1–1)	0.786 (0.200–0.921)	1 (1–1)	1 (1–1)	1 (1–1)	1 (1–1)
	0.209 (0.033–0.385)	0.422 (−0.118 to 0.963)	0.919 (0.200–0.936)	0.422 (−0.107 to 0.892)	0.302 (0.207–0.870)	0.451 (0.200–0.947)	0.433 (0.118–0.899)
SVM	0.999 (0.999–1)	1 (1–1)	0.668 (0.417–0.732)	1 (1–1)	1 (1–1)	1 (1–1)	1 (1–1)
	0.548 (0.092–1)	0.489 (0.108–0.869)	0.725 (0.417–0.735)	0.503 (0.108–0.787)	0.399 (0.080–0.969)	0.601 (0.100–0.799)	0.555 (0.302–0.699)

T2WI, T2-weighted imaging; DWI, diffusion-weighted imaging; DCE, dynamic contrast-enhanced; LR, logistic regression; BDT, bagging decision tree; DT, decision tree; GP, Gaussian process; SVM, support vector machine.

Intratumoral radiomics predicts the value of microsatellite instability

By applying six classifiers to the three MRI sequences and their combinations, a total of 42 intratumoral radiomics models were constructed (Table 4). Among the single-sequence models, the CE sequence demonstrated the most robust predictive performance, yielding an AUC of 0.912 in the training cohort and 0.856 in the test cohort. Furthermore, the combined model incorporating T2WI, DWI, and CE sequences outperformed all single-sequence models, achieving the highest diagnostic efficacy with AUCs of 0.934 and 0.914 in the training and test cohorts, respectively (Table 5).

Peritumoral radiomics predicts microsatellite instability value

A total of 54 peritumoral radiomics models were constructed by applying six classifiers to three peritumoral ROIs (Table 5). The analysis revealed that peritumoral imaging features generally demonstrated favorable predictive value in the test cohort. Specifically, models derived from the 3-mm peritumoral margin of T2WI, DWI, and CE sequences exhibited robust performance. Among these, the DWI 3-mm model yielded the most superior diagnostic efficacy, achieving an AUC of 0.898 in the training cohort and 0.790 in the test cohort.

The value of intratumoral and peritumoral radiomics in predicting microsatellite instability

In this study, we developed combined radiomics models by integrating intratumoral features with the optimal peritumoral features for each MRI sequence and their multiparametric combination (Figure 3). These selected features were input into a BDT classifier. The results demonstrated that the combined intratumoral–peritumoral models consistently yielded higher AUC values than the standalone intratumoral or peritumoral models across all sequences (Table 6). Notably, the multiparametric fusion model (T2WI + DWI + CE + DWI 3 mm) exhibited the most superior predictive performance, achieving an AUC of 0.998 in the test cohort (Figure 3f). Furthermore, the calibration curve indicated excellent concordance between predicted probabilities and observed outcomes in the training cohort (Figure 4). The DeLong test confirmed that the improvement in AUC for the combined model was statistically significant compared with its corresponding single-region models ($P < 0.05$, Table 7).

Table 5. Area Under the Receiver Operating Characteristic Curve of 54 Peri-Tumoral Radiomic features in the Training Group and the Test Group

Model	LR		BDT		DT		GP		SVM	
	Train	Test	Train	Test	Train	Test	Train	Test	Train	Test
T2WI										
3 mm	0.354 (0.726–0.782)	0.438 (0.072–0.697)	0.863 (0.775–0.990)	0.897 (0.789–0.899)	0.4194 (0.3071–0.5316)	0.704 (0.416–0.8501)	0.677 (0.219–1)	0.831 (0.401–1)	0.548 (0.092–1)	0.389 (0.287–1)
5 mm	0.719 (0.214–0.745)	0.719 (0.219–0.745)	0.831 (0.675–0.963)	0.857 (0.789–0.947)	0.950 (0.435–1)	0.409 (0.405–1)	0.713 (0.329–0.810)	0.677 (0.389–0.809)	0.725 (0.4172–0.735)	0.309 (0.044–0.598)
7 mm	0.632 (0.108–0.698)	0.509 (0.108–0.830)	0.567 (0.389–0.745)	0.741 (0.618–0.897)	0.809 (0.509–1)	0.350 (0.339–1)	0.810 (0.709–0.880)	0.590 (0.300–0.745)	0.601 (0.306–0.823)	0.742 (0.010–0.770)
DWI										
3 mm	0.475 (0.463–0.901)	0.554 (0.178–0.801)	0.898 (−0.186–1)	0.790 (0.782–1)	0.794 (0.609–0.821)	0.530 (0.507–0.712)	0.782 (0.238–1)	0.590 (0.409–1)	0.684 (0.292–1)	0.690 (0.163–0.773)
5 mm	0.803 (0.306–0.887)	0.598 (0.023–0.862)	0.801 (0.772–0.987)	0.689 (0.789–0.983)	0.950 (0.435–1)	0.689 (0.2980.891)	0.782 (0.238–1)	0.59 (0.583–0.901)	0.672 (0.538–0.798)	0.725 (0.417–0.735)
7 mm	0.555 (0.207–0.801)	0.919 (0.601–1)	0.767 (0.629–0.899)	0.790 (0.690–0.909)	0.801 (0.643–0.900)	0.550 (0.435–0.670)	0.702 (0.419–0.721)	0.809 (0.509–1)	0.672 (0.507–0.676)	0.599 (0.392–0.821)
DCE										
3 mm	0.589 (0.508–0.794)	0.608 (0.598–0.904)	0.868 (0.798–0.921)	0.798 (0.655–0.900)	0.899 (0.862–1)	0.530 (0.521–0.789)	0.679 (0.539–0.809)	0.481 (0.439–0.801)	0.731 (0.529–0.901)	0.791 (0.700–0.875)
5 mm	0.698 (0.014–0.890)	0.978 (0.649–0.995)	0.569 (0.721–1)	0.743 (0.721–1)	0.809 (0.710–0.830)	0.671 (0.189–0.891)	0.733 (0.029–0.880)	0.567 (0.509–0.590)	0.698 (0.692–0.901)	0.773 (0.691–0.887)
7 mm	0.190 (0.043–0.699)	0.341 (0.240–0.801)	0.833 (0.721–1)	0.734 (0.721–1)	0.753 (0.693–0.917)	0.510 (0.419–0.786)	0.701 (0.328–0.759)	0.509 (0.512–0.798)	0.729 (0.109–0.781)	0.591 (0.478–0.830)

T2WI, T2-weighted imaging; DWI, diffusion-weighted imaging; DCE, dynamic contrast-enhanced; LR, logistic regression; BDT, bagging decision tree; DT, decision tree; GP, Gaussian process; SVM, support vector machine.

Discussion

By aggregating complementary information from three MRI sequences, we effectively captured multidimensional tumor heterogeneity: DWI characterizes cellular density, T2WI discriminates tissue anatomy, and CE reflects tumor vascularity. Although numerous studies have demonstrated the utility of MRI-based models in predicting MSI, most have focused exclusively on the intratumoral volume, often overlooking the critical information provided by the peritumoral region regarding tumor invasiveness and biological behavior.[16-20] The peritumoral region serves as a critical interface for tumor–host interaction. At the microscopic level, this zone encompasses not only tumor cells but also immune cells within the tumor microenvironment, both of which play pivotal roles in tumorigenesis and progression. Recent studies have successfully combined intratumoral and peritumoral radiomics to evaluate HER2 status in breast cancer,[21] predict chemotherapy response in lung adenocarcinoma,[22] grade gliomas,[23] and assess ablation effects in lung malignancies,[24] all yielding promising results. Building on this evidence and considering anatomical constraints, our study defined peritumoral ROIs expanding 3, 5, and 7 mm from the tumor margin, strictly excluding the uterine serosa, cystic changes, and hemorrhage. These margins were selected to effectively capture early pathological changes—such as micro-infiltration, inflammatory responses, and angiogenesis—while minimizing noise from healthy tissue. Our results indicated that among single-sequence intratumoral models, CE demonstrated the most robust predictive performance (training AUC: 0.912; test AUC: 0.856). Furthermore, the multiparametric model (T2WI+DWI+CE) achieved the highest overall diagnostic efficacy (training AUC: 0.934; test AUC: 0.914). These findings corroborate the work of Zhao et al.,[14] who reported similar performance for a combined T2WI, CE, and DWI model in predicting EC-MSI (training AUC: 0.912; test AUC: 0.907). Both studies suggest that integrating multiple sequences provides a comprehensive

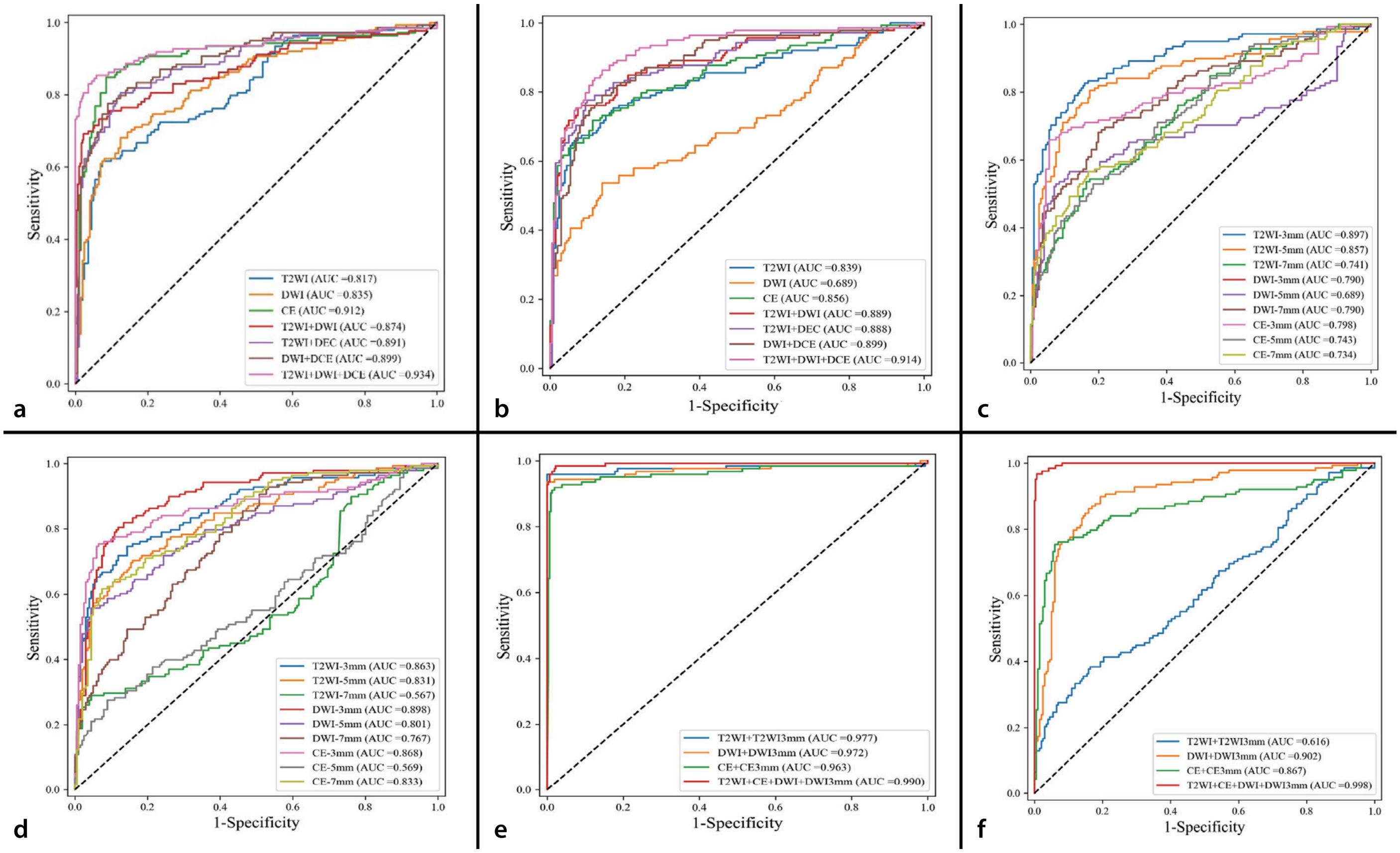

Figure 3. ROC curves of intratumoral, peritumoral, and intratumoral + peritumoral radiomics models in each sequence. **(a)** Training cohort intratumoral; **(b)** test cohort intratumoral; **(c)** training cohort peritumoral; **(d)** test cohort peritumoral; **(e)** training cohort intratumoral + optimal peritumoral and optimal intratumoral + optimal peritumoral; **(f)** test cohort intratumoral + optimal peritumoral and optimal intratumoral + optimal peritumoral. ROC, receiver operating characteristic; T2WI, T2-weighted imaging; DWI, diffusion-weighted imaging; CE, contrast-enhanced; AUC, area under the curve.

Table 6. Prediction efficacy of intratumoral + best peritumoral and best intratumoral + best peritumoral models

Model	Train				Test			
	AUC (95% CI)	SEN	SPE	ACC	AUC (95% CI)	SEN	SPE	ACC
T2WI + T2WI 3 mm	0.977 (0.954–0.999)	0.436	1	0.929	0.616 (0.241–0.991)	0.521	0.931	0.818
DWI + DWI 3 mm	0.972 (0.907–1)	0.801	0.943	0.809	0.902 (0.765–0.943)	0.776	0.854	0.808
CE + CE 7 mm	0.963 (0.932–0.994)	0.2857	1	0.921	0.867 (0.694–1)	0.333	0.965	0.906
T2WI + CE + DWI + DWI 3 mm	0.990 (0.964–1)	0.818	1	0.921	0.998 (0.941–1)	0.670	0.8276	0.727

T2WI, T2-weighted imaging; DWI, diffusion-weighted imaging; CE, contrast-enhanced; AUC, area under the curve; CI, confidence interval; ACC, accuracy; SEN, sensitivity; SPE: specificity.

Table 7. DeLong test

Model	AUC	SEN	SPE	ACC
Intra vs. intra and peri	0.002	0.500	0.625	0.688
Peri vs. intra	0.878	1.000	1.000	0.500
Intra and peri vs. intra	0.031	0.500	0.625	0.688

Intra, intra-tumor; Peri, peri-tumor; AUC, area under the curve; ACC, accuracy; SEN, sensitivity; SPE: specificity.

assessment of tumor malignancy and heterogeneity. We attribute the superior performance of CE-based models to their ability to reflect tumor vascularity and permeability, which aligns with recent findings[25] suggesting that CE imaging holds significant potential for prognostication in EC.

Our analysis of the peritumoral region revealed that radiomic features extracted from the peritumoral margin possess significant predictive value. Specifically, the 3-mm peritumoral regions across T2WI, DWI, and CE sequences all demonstrated favorable efficacy. Among these, the DWI 3 mm model exhibited the most robust performance, achieving AUCs of 0.898 in the training cohort and 0.790 in the test cohort. Notably, this peritumoral performance surpassed that of certain intratumoral models, underscoring the critical role of peritumoral heterogeneity as a supplementary biomarker for MSI status. These findings align with recent observations in hepatocellular carcinoma

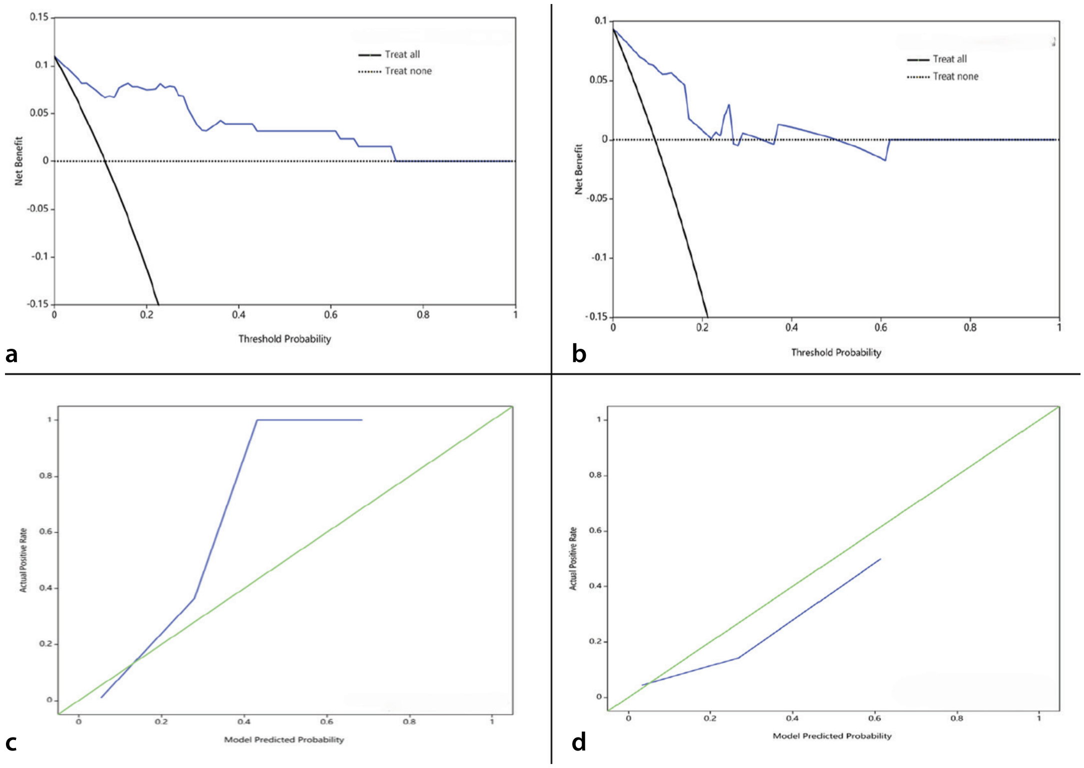

Figure 4. Optimal model DCA curves and calibration curves. **(a)** DCA curve of the training cohort; **(b)** DCA curve of the test cohort; **(c)** calibration curve of the training cohort; **(d)** calibration curve of the test cohort. DCA, decision curve analysis.

research.[26,27] To further enhance diagnostic accuracy, we developed combined models integrating the optimal intratumoral and peritumoral features. Consistent with our hypothesis, the fusion models universally outperformed their corresponding single-region counterparts (intratumoral only or peritumoral only). The most impressive results were obtained from the multiparametric fusion model, which combined intratumoral features from T2WI, DWI, and CE sequences with the optimal peritumoral DWI 3-mm features. This comprehensive model yielded the highest diagnostic efficacy, with AUCs reaching 0.990 and 0.998 in the training and test cohorts, respectively.

Radiomics is a promising high-throughput methodology capable of quantitatively characterizing micro-architectural heterogeneity and structural patterns within medical images, thereby generating novel imaging biomarkers.[28,29] In this study, we extracted radiomic features from the primary tumor and its surrounding 3-, 5-, and 7-mm margins to facilitate a non-invasive virtual biopsy.[30] Our findings revealed a high degree of complementarity between intratumoral and peritumoral features for the preoperative prediction of MSI in EC. This suggests that the peritumoral microenvironment harbors critical biological insights that effectively compensate for the information limitations inherent in analyzing the gross tumor volume alone. Concurrently, advancements in artificial intelligence have enabled the precise screening and efficient integration of high-dimensional radiomics data, expanding the horizon of clinical applications.[31] We employed five distinct machine learning algorithms to identify the optimal predictive model. The BDT emerged as the most robust classifier. Although its performance varied slightly across cohorts, it demonstrated superior stability and generalization capabilities. Mechanistically, BDT enhances classification accuracy by aggregating predictions from multiple DTs. This ensemble approach effectively reduces variance and mitigates the risk of overfitting,[32] thereby providing reliable decision support for the prognostic stratification and clinical management of patients with EC.

This study is subject to certain limitations. First, as a retrospective single-center study, the sample size was relatively modest, which may inherently introduce selection bias. Second, our analysis was restricted to standard clinical MRI sequences. Although effective, the inclusion of advanced functional imaging techniques could potentially offer deeper physiological insights into tumor heterogeneity and further refine predictive accuracy. To address these limitations, future research should adopt a multi-center, large-scale, prospective design. Collaborating across multiple institutions will facilitate the inclusion of a diverse patient population and allow for validation across different MRI scanning platforms and standardized protocols. Such efforts are essential to enhance the generalizability and robustness of the predictive model for broader clinical application.

In conclusion, this study leveraged multiparametric MRI to extract and analyze radiomic features from both intratumoral and peritumoral regions. By employing machine learning algorithms for optimal feature selection, we constructed an integrated intratumoral–peritumoral radiomics model that demonstrated superior diagnostic efficacy in predicting the MSI status of patients with EC. With accuracy comparable to the gold-standard postoperative IHC, this model serves as a reliable, non-invasive imaging tool to guide personalized preoperative treatment planning and prognostic assessment for patients with EC.

Footnotes

Conflict of interest disclosure

This study was supported in part by grants from the Llinchuang Foundation of First Affiliated Hospital of Medical College, Shihezi University (Grant number: LC2025019).

References

1. Sung H, Ferlay J, Siegel RL, et al. Global Cancer Statistics 2020: GLOBOCAN estimates of incidence and mortality worldwide for 36 cancers in 185 countries. *CA Cancer J Clin*. 2021;71(3):209-249. [Crossref]
2. Li K, Luo H, Huang L, Luo H, Zhu X. Microsatellite instability: a review of what the oncologist should know. *Cancer Cell Int*. 2020;20:16. [Crossref]
3. Antill Y, Kok PS, Robledo K, et al. Clinical activity of durvalumab for patients with advanced mismatch repair-deficient and repair-proficient endometrial cancer. A nonrandomized phase 2 clinical trial. *J Immunother Cancer*. 2021;9(6):e002255. [Crossref]
4. Song Y, Gu Y, Hu X, Wang M, He Q, Li Y. Endometrial tumors with MSI-H and dMMR share a similar tumor immune microenvironment. *Onco Targets Ther*. 2021;14:4485-4497. [Crossref]
5. Yang YS, Long X, Du XM, Fan WX, Zhang TH. The value of preoperative MR ADC in predicting microsatellite instability status in endometrial carcinoma. *J China Clin Med Imaging*. 2025;36(5):353356. [Crossref]
6. Ren JP, Zhang M, Liu WY. Assessing microsatellite instability of endometrial adenocarcinoma with multimodal intravoxel incoherent motion MRI. *International Journal of Medical Radiology*. 2023;46(4):396-401. [Crossref]
7. Pan MY, Cai WZ, Chen L, Wen J. Establishment of microsatellite instability assessment model for endometrial carcinoma by clinic-imaging omics. *Journal of Molecular Imaging*. 2023;46(1):48-52. [Crossref]
8. Ma CJ, Tian SF, Chen LH, et al. Quantitative assessment of microsatellite instability in endometrial cancer by T2 mapping combined with mDixon-Quant multiparameter imaging. *Chinese Journal of Magnetic Resonance Imaging*. 2022;13(8):48-54. [Crossref]
9. Tian SF, Liu AL, Chen LH, et al. Evaluation of microsatellite instability in endometrial carcinoma by amide proton transfer imaging and diffusion kurtosis imaging. *Journal of China Clinic Medical Imaging*. 2022;33(5):345-349. [Crossref]
10. Aerts HJWL, Velazquez ER, Leijenaar RTH, et al. Correction: corrigendum: decoding tumour phenotype by noninvasive imaging using a quantitative radiomics approach. *Nat Commun*. 2014;5:4644. [Crossref]
11. Bera K, Braman N, Gupta A, Velcheti V, Madabhushi A. Predicting cancer outcomes with radiomics and artificial intelligence in radiology. *Nat Rev Clin Oncol*. 2022;19(2):132-146. [Crossref]
12. Liu ZY, Ding YX, Bai GJ. Prediction of endometrial cancer microsatellite expression status via deep transfer learning features based on multi-parameter MRI. *Chin J Med Imaging*. 2025;33(5):546-552,561. [Crossref]
13. Niu YC, Zhou F, Zhao DD, Hou MY, Li JS, Zhang Y. Value of a prediction model based on DWI deep learning features for evaluating microsatellite instability status in endometrial cancer. *Chin J Med Imaging*. 2024;32(9):922-927. [Crossref]
14. Zhao JF, Tian Y, Ma MM, Cao XS. Application research of imaging genomics in preoperative prediction of microsatellite stability of endometrial cancer using mp-MRI. *Chin J Magn Reson Imaging*. 2024;15(11):110-116,122. [Crossref]
15. Jiang M, Jia K, Wang L, et al. Alterations of DNA damage response pathway: Biomarker and therapeutic strategy for cancer immunotherapy. *Acta Pharm Sin B*. 2021;11(10):2983-2994. [Crossref]
16. Wang Z, Hu Y, Cai J, et al. Potential value of novel multiparametric MRI radiomics for preoperative prediction of microsatellite instability and Ki-67 expression in endometrial cancer. *Sci Rep*. 2025;15:3226. [Crossref]
17. Li Z, Su Y, Cui Y, Yin Y, Li Z. Multi-sequence MRI-based clinical-radiomics models for the preoperative prediction of microsatellite instability-high status in endometrial cancer. *Precis Radiat Oncol*. 2025;9(1):43-53. Erratum in: *Precis Radiat Oncol*. 2025;9(3):228. [Crossref]
18. Zhou L, Zheng L, Hong C, et al. A novel model for predicting microsatellite instability in endometrial cancer: integrating deep learning-pathomics and MRI-based radiomics. *Acad Radiol*. 2025;32(10):5940-5950. [Crossref]
19. Wei QY, Li Y, Huang XL, et al. Predicting microsatellite instability in endometrial cancer by multimodal magnetic resonance radiomics combined with clinical factors. *Acad Radiol*. 2025;32(11):6693-6706. [Crossref]
20. Zhang M, Wang X, Li Z, et al. A radiomics model based on diffusion-weighted imaging developed using machine learning enables prediction of microsatellite instability in endometrial cancer. *BMC Med Imaging*. 2025;25:405. [Crossref]
21. Li ZJ, Yang XF, Jiang ZY, et al. Intratumoral and peritumoral radiomics assessment of HER2 status in breast cancer based on DBT. *J Clin Radiol*. 2023;42(9):1436-1441. [Crossref]
22. Khorrami M, Khunger M, Zagouras A, et al. Combination of peri- and intratumoral radiomic features on baseline CT scans predicts response to chemotherapy in lung adenocarcinoma. *Radiol Artif Intell*. 2019;1(2):e180012. [Crossref]
23. Liu SZ, Wang ZB, Lou J, Jiang F, Xia XS. Prediction of glioma pathologic grading based on multisequence peritumor and intratumor radiomics. *Clin Radiol J*. 2024;43(9):14501455. [Crossref]
24. Zhu Fandong, Yang Chen, Zou Jiajun, Liu Xuefeng, Zhang Wei, Li Jun, Chen Hui, Wang Lei. Based on peritumoral CT radiomics may assess the early efficacy of microwave ablation in lung malignant tumors. *J Clin Radiol*. 2023;42(8):1317-1321. [Crossref]
25. Zhang Y, Bao X, Wang Y, Li L, Liu L, Wu Q. Machine learning-based radiomics model: prognostic prediction and mechanism exploration in patients with endometrial cancer. *Biomark Res*. 2025;13(1):119. [Crossref]
26. Wang F, Cheng M, Du B, et al. Predicting microvascular invasion in small (≤5 cm) hepatocellular carcinomas using radiomics-based peritumoral analysis. *Insights Imaging*. 2024;15(1):90. [Crossref]
27. Zhao Y, Zhang J, Wang N, et al. Intratumoral and peritumoral radiomics based on contrast-enhanced MRI for preoperatively predicting treatment response of transarterial chemoembolization in hepatocellular carcinoma. *BMC Cancer*. 2023;23(1):1026. [Crossref]
28. Greten TF, Villanueva A, Korangy F, et al. Biomarkers for immunotherapy of hepatocellular carcinoma. *Nat Rev Clin Oncol*. 2023;20(11):780-798. [Crossref]
29. Zhang Z, Wan X, Lei X, et al. Intra- and peri-tumoral MRI radiomics features for preoperative lymph node metastasis prediction in early-stage cervical cancer. *Insights Imaging*. 2023;14(1):65. [Crossref]
30. Roussel E, Capitanio U, Kutikov A, et al. Novel imaging methods for renal mass characterization: a collaborative review. *Eur Urol*. 2022;81(5):476-488. [Crossref]
31. Chen M, Copley SJ, Viola P, Lu H, Aboagye EO. Radiomics and artificial intelligence for precision medicine in lung cancer treatment. *Semin Cancer Biol*. 2023;93:97-113. [Crossref]
32. Shoeibi A, Sadeghi D, Moridian P, et al. Automatic diagnosis of schizophrenia in EEG signals using CNN-LSTM models. *Front Neuroinform*. 2021;15:777977. [Crossref]